JACS
JOURNAL OF THE AMERICAN CHEMICAL SOCIETY
Article
pubs.acs.org/JACS

A New Water Oxidation Catalyst: Lithium Manganese Pyrophosphate with Tunable Mn Valency

Jimin Park,[†,∥] Hyunah Kim,[†,∥] Kyoungsuk Jin,[†] Byung Ju Lee,[†] Yong-Sun Park,[†] Hyungsub Kim,[†] Inchul Park,[†] Ki Dong Yang,[†] Hui-Yun Jeong,[†] Jongsoon Kim,[†] Koo Tak Hong,[†,‡] Ho Won Jang,[†,‡] Kisuk Kang,*[,†,‡,§] and Ki Tae Nam*[,†,‡]

[†]Department of Materials Science and Engineering, [‡]Research Institute of Advanced Materials (RIAM), and [§]Center for Nanoparticle Research, Institute for Basic Science (IBS), Seoul National University, 1 Gwanak-ro, Gwanak-gu, Seoul 151-742, Republic of Korea

Supporting Information

ABSTRACT: The development of a water oxidation catalyst has been a demanding challenge for the realization of overall water-splitting systems. Although intensive studies have explored the role of Mn element in water oxidation catalysis, it has been difficult to understand whether the catalytic capability originates mainly from either the Mn arrangement or the Mn valency. In this study, to decouple these two factors and to investigate the role of Mn valency on catalysis, we selected a new pyrophosphate-based Mn compound ($Li_2MnP_2O_7$), which has not been utilized for water oxidation catalysis to date, as a model system. Due to the monophasic behavior of $Li_2MnP_2O_7$ with delithiation, the Mn valency of $Li_{2-x}MnP_2O_7$ (x = 0.3, 0.5, 1) can be controlled with negligible change in the crystal framework (e.g., volume change ~1%). Moreover, inductively coupled plasma mass spectrometry, X-ray photoelectron spectroscopy, ex-situ X-ray absorption near-edge structure, galvanostatic charging−discharging, and cyclic voltammetry analysis indicate that $Li_{2-x}MnP_2O_7$ (x = 0.3, 0.5, 1) exhibits high catalytic stability without additional delithiation or phase transformation. Notably, we observed that, as the averaged oxidation state of Mn in $Li_{2-x}MnP_2O_7$ increases from 2 to 3, the catalytic performance is enhanced in the series $Li_2MnP_2O_7$ < $Li_{1.7}MnP_2O_7$ < $Li_{1.5}MnP_2O_7$ < $LiMnP_2O_7$. Moreover, $Li_2MnP_2O_7$ itself exhibits superior catalytic performance compared with MnO or MnO_2. Our study provides valuable guidelines for developing an efficient Mn-based catalyst under neutral conditions with controlled Mn valency and atomic arrangement.

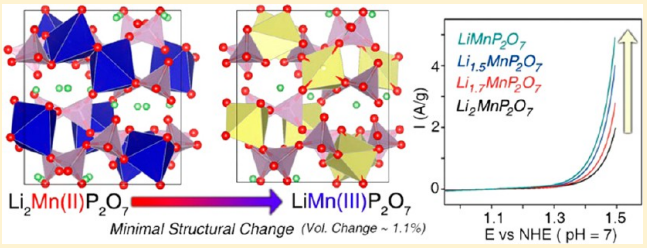

1. INTRODUCTION

Splitting water to generate hydrogen and oxygen molecules is an environmentally friendly solar-to-energy conversion method.[1−8] The oxygen evolution reaction (OER) has been regarded as a rate-limiting step in realizing a fully integrated water-splitting system because of the high energy barrier for O−O bond formation.[9−11] Precious metal oxides, such as RuO_2 and IrO_2, exhibit superb OER catalytic activity;[12−17] however, their high price remains an unavoidable weakness. Therefore, the development of efficient, durable, and inexpensive alternative catalysts is desirable.

Interestingly, nature has a water oxidation complex (WOC) in photosystem II comprised of earth-abundant Mn and Ca that generates oxygen efficiently under neutral conditions.[18−20] Inspired by the Mn_4CaO_5 cluster in the WOC, various crystalline manganese oxide polymorphs[21−26] and amorphous MnO_x[27,28] have been investigated as water oxidation catalysts and have demonstrated superior catalytic performance under basic conditions. However, unlike the WOC in nature, the catalytic properties of Mn oxide compounds degrade drastically at neutral pH.[29−31] Accordingly, extensive research efforts have been spent on exploring for manganese-based chemistry that is catalytically active even at neutral conditions.[28,29]

Previous works on manganese-containing catalysts have experimentally and theoretically emphasized the role of Mn(III) as an important intermediate state to enable the catalytic reaction.[27−29,32] Irrespective of the initial manganese oxidation states in catalysts, Mn(III) is generated and participates in the water oxidation process.[29] However, considering the electronic configuration, Mn(III) (t_{2g}^3 e_g^1) accompanies strong Jahn−Teller distortion and tends to break the symmetry of the orbitals;[22,25,29] thus, this state is not stable in symmetric octahedral structures.[29,32] In this respect, many previous studies have suggested that the degradation of manganese-based catalysts results from Mn(III) disproportionation into Mn(II) and Mn(IV) in neutral water, losing its catalytic property.[29]

On the basis of such a theoretical approach, there have been many pioneering studies to stabilize Mn(III) and to understand the role of manganese ions to enhance catalytic activity.[22,28,29,32] For example, the Nakamura group stabilized the Mn(III) state by introducing partial asymmetry to the crystal field in MnO_2 through nitrogen doping, and promoted the water catalysis of MnO_2.[32] The Dau group synthesized

Received: October 4, 2013
Published: February 26, 2014

dx.doi.org/10.1021/ja410223j | J. Am. Chem. Soc. 2014, 136, 4201−4211

amorphous Mn oxide films with distorted, corner-sharing MnO_6 octahedra to stabilize Mn(III) sites.[28] Moreover, the effect of manganese crystal environments on the catalytic role was recently investigated by the Dismukes group.[22] They comparatively studied eight different manganese oxides, including Mn_2O_3, Mn_3O_4, β-MnO_2, λ-MnO_2, and $LiMn_2O_4$, and found that the catalytic activity generally enhances when Mn−O bonds are weak/distorted and Mn−Mn distances are long in the structure.[22] It was also shown that $LiMn_2O_4$ composed of Mn(III) and Mn(IV) atoms has no catalytic activity, while λ-MnO_2, which does not contain Mn(III) atoms, exhibits high catalytic activity.[22] All of these works suggest that not only Mn valency but also structural factors, such as the crystal framework and the Mn geometry, are mutually important in determining the catalytic activity.

However, in understanding the catalytic activities of these manganese-based compounds, it seems not trivial to decouple the effect of the Mn valency and structural factors. Typically, the crystal systems of Mn(III)-containing oxides are different from those of Mn(IV)- or Mn(II)-based oxides. Thus, comparing these two systems with different manganese oxidation states inevitably involves the influence of the manganese local environments in each crystal system.[22,33] A question that we attempt to understand in this study is whether the catalytic property will change with the variation of Mn valency when the same structural factors are maintained. We decoupled the two factors and obtained a clue to understanding how Mn valency affects water catalysis. Herein, we have selected $Li_2MnP_2O_7$ as a model system. The notable capability of $Li_2MnP_2O_7$ is that the oxidation state of Mn can be accurately adjusted from 2 to 3 by controlled delithiation with minimum structural change.[34] Other manganese oxide/phosphate-based lithium intercalation materials typically undergo significant phase separation or transformation during delithiation.[35,36] For example, $LiMnPO_4$ phase separates into $LiMnPO_4$ and $MnPO_4$ upon delithiation.[35] $LiMn_2O_4$ also transforms by two-phase reaction into $Li_{0.5}Mn_2O_4$ or λ-MnO_2 during delithiation.[36] Another reason why we chose $Li_2MnP_2O_7$ as a catalyst is that the pyrophosphate group itself has unique advantages in distorting Mn geometry due to its asymmetric nature.[37−40] While it is hard to achieve with conventional Mn oxide compounds,[33] a distorted local crystal structure in $Li_2MnP_2O_7$ is expected to be favorable for the catalytic cycle.[28,32,41] Moreover, the pyrophosphate group has been used as a stabilizing agent for the Mn(III) state via specific chelating reactions under neutral pH.[29,42]

2. RESULTS AND DISCUSSION

A $Li_2MnP_2O_7$ compound was synthesized using a previously reported conventional solid-state method.[34] A stoichiometric amount of Li_2CO_3, $MnC_2O_4{\cdot}2H_2O$, and $(NH_4)_2HPO_4$ was initially mixed by planetary milling for 12 h. Then, the mixture was initially heated at 300 °C for 6 h and heated again at 600 °C for 10 h under steady Ar flow to produce the $Li_2MnP_2O_7$ compound. The X-ray diffraction (XRD) pattern of the synthesized compound matches well with the previously reported pattern of $Li_2MnP_2O_7$ (Figure 1a). Close observation of the $Li_2MnP_2O_7$ crystal allows us to distinguish two different manganese sites in one unit cell: one is a trigonal bipyramidal (TBP) (MnO_5), and the other is octahedral (Oh) (MnO_6). The TBP and Oh polyhedrons formed M_2O_9 subunits by edge-sharing coordination. As illustrated in Figure 1b, the surrounding geometry of each manganese atom is symmetrically broken, and the M_2O_9 subunits are interconnected through bulky P_2O_7 groups to form the three-dimensional framework structures. The asymmetric geometry of each manganese atom can be clearly observed by measuring the distances and angles between the manganese and oxygen atoms. The TBP polyhedron has various O−Mn−O angles and Mn−O distances ranging from 82.61° to 152.17° and from 2.117 to 2.246 Å, respectively. The Oh polyhedron also exhibits an asymmetric geometry, with the O−Mn−O angles and Mn−O distances ranging from 82.47° to 110.65° and from 2.119 to 2.308 Å, respectively. Additionally, the shortest Mn−Mn distance is 3.302 Å, and the second shortest Mn−Mn distance is 5.010 Å, which are longer than any other manganese oxides[22,33,40] due to the bulky P_2O_7 groups that interconnects manganese polyhedrons.

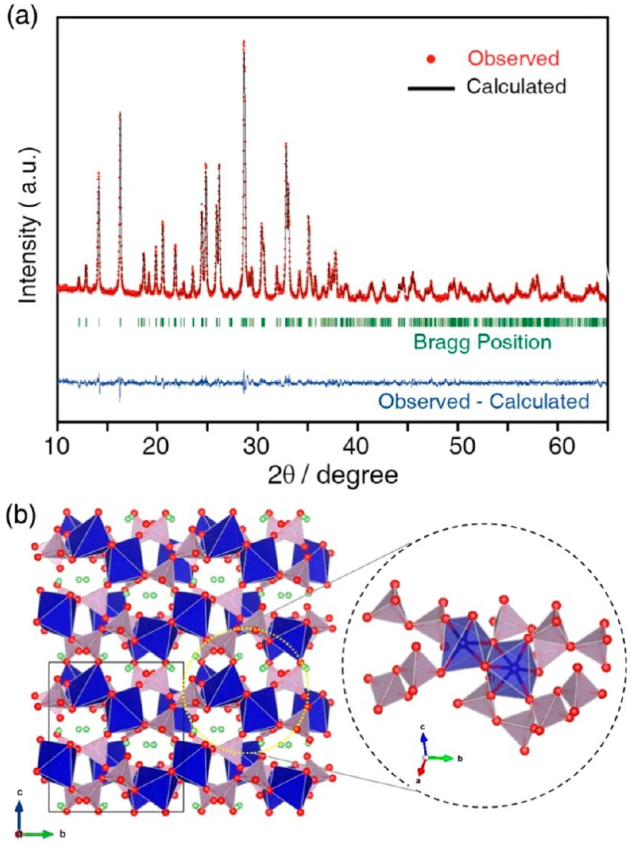

Figure 1. (a) Rietveld refinement pattern of high-resolution X-ray diffraction data for $Li_2MnP_2O_7$: red dots, experimental data points; the black line, calculated powder pattern; the green ticks, Bragg positions; and the blue line, difference between the observed and calculated patterns. R_P = 1.59%, R_{WP} = 2.07%, R_I = 0.956%, R_F = 1.22%, χ^2 = 2.11. (b) Crystal structure of $Li_2MnP_2O_7$. The inset shows the local environment around the Mn_2O_9 subunit (blue). The pyrophosphate units and Li atoms are depicted in gray and green, respectively.

To understand the effect of Mn valency on the OER, we attained $LiMnP_2O_7$, $Li_{1.5}MnP_2O_7$, and $Li_{1.7}MnP_2O_7$ compounds by removing Li^+ ions from $Li_2MnP_2O_7$ powders. $Li_2MnP_2O_7$ was chemically delithiated using NO_2BF_4 according to the following reaction:

$$Li_2MnP_2O_7 + xNO_2BF_4 \rightarrow Li_{2-x}MnP_2O_7 + xLiBF_4 + xNO_2$$

dx.doi.org/10.1021/ja410223j | J. Am. Chem. Soc. 2014, 136, 4201−4211

NO_2BF_4 was used as a strong oxidizing agent with a redox potential for NO_2^+/NO_2 of 2.05 V versus NHE (5.1 V versus Li^+/Li).[43] As the amount of NO_2BF_4 increased, the averaged Mn valency in $Li_{2-x}MnP_2O_7$ gradually changed from 2 to 3. There was no significant change in the morphology, size, and surface area arising from the delithiation, as observed by TEM and BET analysis (Figure S1, Supporting Information).

XRD, X-ray photoelectron spectroscopy (XPS), and ex-situ X-ray absorption near-edge structure (XANES) analysis of $Li_{2-x}MnP_2O_7$ (x = 0, 0.3, 0.5, 1) was performed to probe the gradual delithiation and Mn valency change. The delithiation process in $Li_2MnP_2O_7$ proceeds in a monophasic manner, accompanying a continuous peak shift without any appearance or disappearance of the peak (Figure 2a and inset). For example, the (110) peak continuously shifts from 14.10° to 14.01°, and the (002) peak also shifts from 16.27° to 16.18°. Each XRD pattern was analyzed by full pattern matching, and the corresponding lattices were refined. The variation of the lattice parameter and unit-cell volume as a function of Li content in $Li_{2-x}MnP_2O_7$ (x = 0–1) is demonstrated in Figure 2b. During the delithiation process, the lattice parameters and unit-cell volume expand. However, it should be noted that the change is only ~1%, which implies the minimal change in the overall crystal structure. The ex-situ XANES Mn K-edge spectra of $Li_{2-x}MnP_2O_7$ (x = 0, 0.3, 0.5, 1) powders shift toward a higher energy as more Li ions are removed from $Li_2MnP_2O_7$, indicating the gradual oxidation of the averaged oxidation state of Mn from 2 to 3 during the delithiation (Figure 3a).

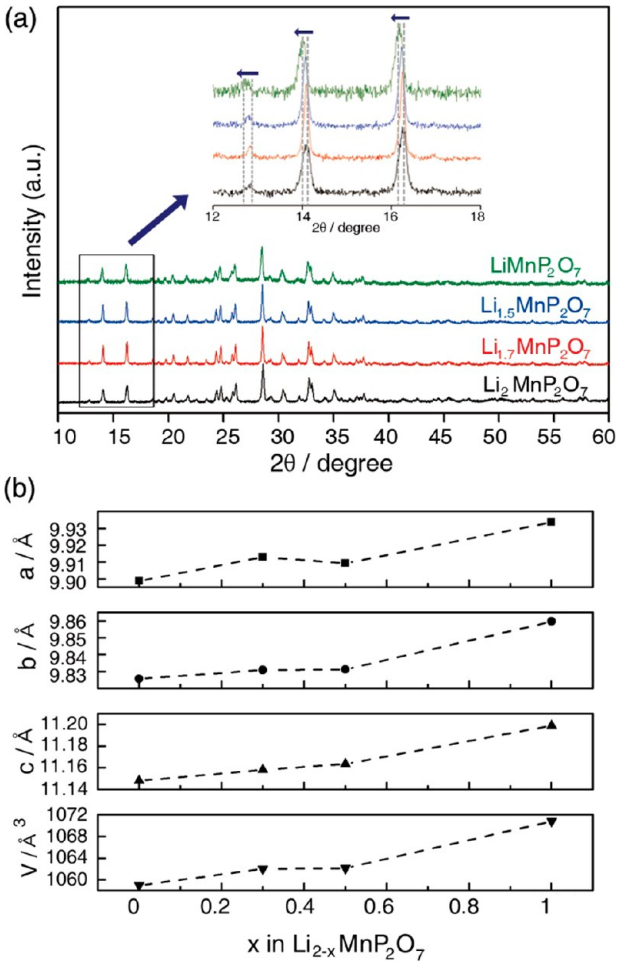

Figure 2. (a) Powder XRD patterns of $Li_2MnP_2O_7$ (black), $Li_{1.7}MnP_2O_7$ (red), $Li_{1.5}MnP_2O_7$ (blue), and $LiMnP_2O_7$ (green). The inset reveals the gradual peak shift during delithiation. (b) The change in the lattice parameters, as determined by Rietveld refinement, and the corresponding unit-cell volumes as a function of Li content in $Li_{2-x}MnP_2O_7$ (x = 0.0–1.0).

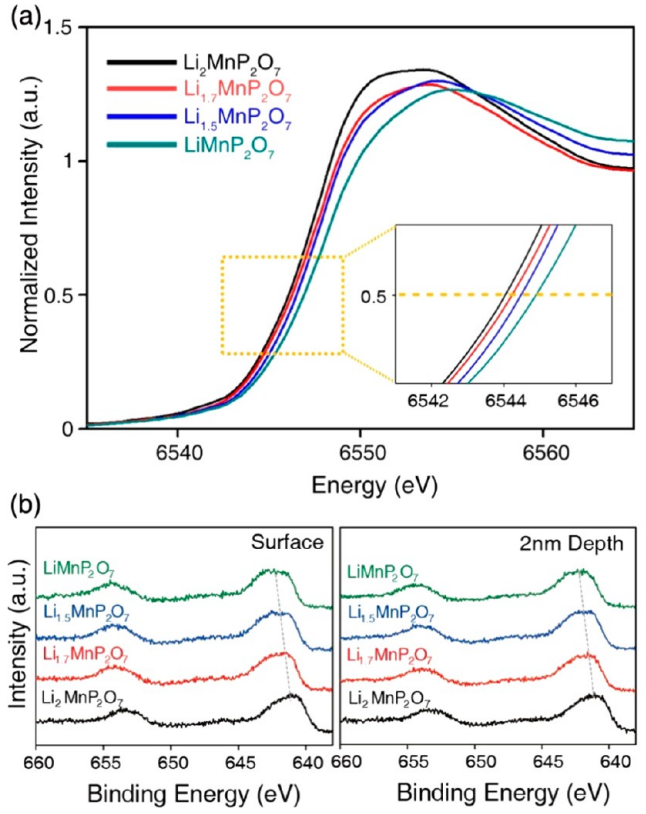

Figure 3. (a) Ex-situ XANES Mn K-edge spectra of $Li_{2-x}MnP_2O_7$ (x = 0, 0.3, 0.5, 1) powders. The inset shows the gradual oxidation of Mn atoms in $Li_{2-x}MnP_2O_7$ (x = 0, 0.3, 0.5, 1) upon delithiation. (b) XPS spectra of the Mn 2p region of $Li_2MnP_2O_7$ (black), $Li_{1.7}MnP_2O_7$ (red), $Li_{1.5}MnP_2O_7$ (blue), and $LiMnP_2O_7$ (green) at the surface (left) and for a 2-nm-etched surface (right).

Additionally, XPS was used to probe the Mn oxidation state at the surface and for 2-nm-etched surfaces of $Li_{2-x}MnP_2O_7$ (x = 0, 0.3, 0.5, 1) by comparing the relative position of the Mn $2p_{1/2}$ peak. In both the surface and 2-nm-etched surfaces of the catalysts, the binding energy of the Mn $2p_{1/2}$ peak increases gradually from 653.2 to 654.5 eV as the Li ion content decreases, confirming the gradual oxidation of Mn upon delithiation (Figure 3b).

The water oxidation catalytic properties of $Li_{2-x}MnP_2O_7$ (x = 0, 0.3, 0.5, 1) were evaluated by cyclic voltammetry under neutral conditions (500 mM sodium phosphate buffer, pH 7.0). Working electrodes were prepared by spin-coating a suspension of catalyst in Nafion solutions onto a FTO (fluorine-doped tin oxide) substrate using a previously reported method.[44,45] The current value was normalized by the total weight or surface area of the catalyst on the working electrode. The total surface area of the catalyst on the substrate was estimated by multiplying the BET (m^2/g) values and the weight of the catalyst (g) on the substrate. For correction of the polarization current, we obtained OER curves by averaging the currents from the forward and reverse cyclic voltammetry (CV scans) [see Figure

dx.doi.org/10.1021/ja410223j | J. Am. Chem. Soc. 2014, 136, 4201–4211

S2 (Supporting Information) for raw CV curves before polarization correction]. Potentiostatic electrolysis of $Li_{2-x}MnP_2O_7$ (x = 0, 0.3, 0.5, and 1) results in a similar current value as the averaged one (Figure S3, Supporting Information). This finding indicates that the averaged current could be a reasonable approximation of the true steady-state current.[46] Notably, we observed that the oxygen evolution ability is enhanced as the averaged Mn oxidation state of the as-prepared catalysts ($Li_{2-x}MnP_2O_7$) increases from 2 to 3. As shown in Figure 4a, the current density of $LiMnP_2O_7$ (5.0 A/g at the overpotential value of 680 mV), in which all the Mn atoms have a trivalent oxidation state, was 2.5 times larger than that of $Li_2MnP_2O_7$ (2.0 A/g at the over potential value of 680 mV), which has only divalent Mn atoms. The current values at the overpotential of 680 mV for $Li_{1.5}MnP_2O_7$ and $Li_{1.7}MnP_2O_7$ were 4.0 and 2.8 A/g, respectively. The enhanced catalytic ability of $Li_{2-x}MnP_2O_7$ upon delithiation was also observed when we normalized the current value to the total surface area of the catalyst (Figure 4a). The same trend of the catalytic activities was also confirmed for the samples mixed with conductive carbon binders (Figure S4, Supporting Information). Moreover, the amount of evolved oxygen molecules during the OER was measured by an Ocean Optics oxygen sensor system according to a previous report. The phase shift of the O_2 sensor on the FOXY probe was converted into the partial pressure of O_2 in the headspace (30 mL). The amount of evolved oxygen was ~4.5 μmol during the electrolysis period of 1 h with a Faradaic efficiency of ~93.8% (Figure S5, Supporting Information).

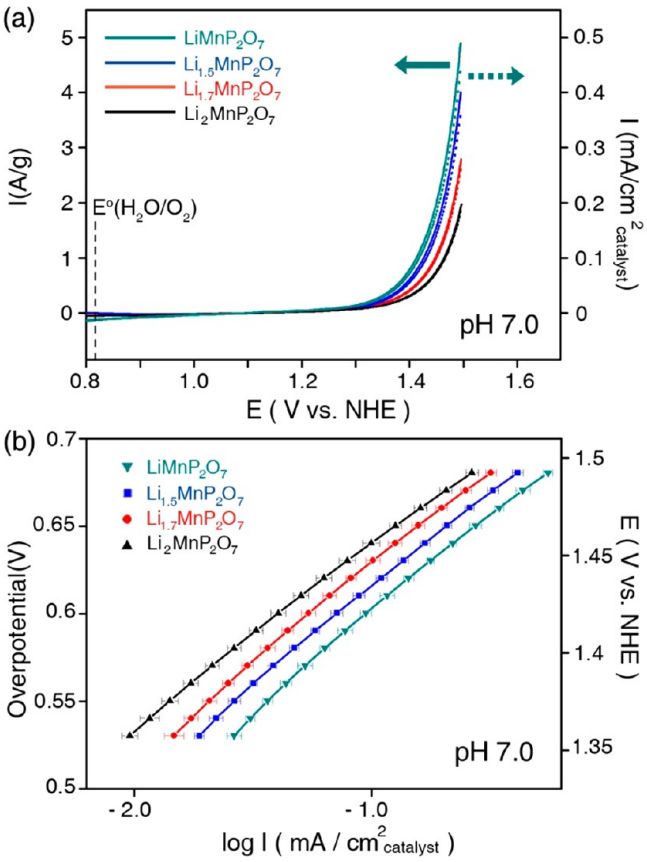

Figure 4. (a) Polarization-corrected cyclic voltammetry curves of $LiMnP_2O_7$ (green), $Li_{1.5}MnP_2O_7$ (blue), $Li_{1.7}MnP_2O_7$ (red), and $Li_2MnP_2O_7$ (black) in 0.5 M sodium phosphate buffer (pH 7.0). The polarization-corrected curves were obtained by averaging the currents of the forward and reverse CV scans. The current value was normalized by the total weight (solid line) and the total surface area of the catalyst (dashed line), respectively. The thermodynamic potential for water oxidation is marked at 0.816 V vs NHE (pH 7). (b) Tafel plots for $LiMnP_2O_7$ (green), $Li_{1.5}MnP_2O_7$ (blue), $Li_{1.7}MnP_2O_7$ (red), and $Li_2MnP_2O_7$ (black) where the current value was normalized by the total surface area of the compounds. The steady-state currents were averaged, and the variations in the currents are indicated by the error bars (n = 10).

We also conducted the same experiments for commercially available MnO (purity 99.99%) and MnO_2 (purity 99.99%) for comparison (Figure S6, Supporting Information). The current values of MnO and MnO_2 at the overpotential value of 680 mV are 0.75 and 0.36 A/g, respectively (Figure S7, Supporting Information). When we normalized the current value to the total surface area of the catalyst, the current densities of MnO and MnO_2 are 64 and 34 $\mu A\ cm^{-2}$, which corresponds well with the previous reports (Figure S7, Supporting Information).[29] According to previous study, the current density of δ-MnO_2 was ~40 $\mu A\ cm^{-2}$ at the overpotential value of 680 mV at pH 7.[29] The current density of $LiMnP_2O_7$ is approximately 6.5 times and 14 times higher than those of MnO and MnO_2, respectively. Moreover, $Li_2MnP_2O_7$ displayed a higher current density than those of MnO_2 and MnO by 6.0 times and 2.5 times, respectively.

A Tafel plot of each catalyst was obtained from steady-state current measurement in which the current was normalized to the total surface area of the catalyst. The steady-state currents were averaged and the variations in the currents are indicated by error bars. As shown in Figure 4b, the exchange current value increased in the series $Li_2MnP_2O_7$ < $Li_{1.7}MnP_2O_7$ < $Li_{1.5}MnP_2O_7$ < $LiMnP_2O_7$. The slopes of all the $Li_{2-x}MnP_2O_7$ (x = 0, 0.3, 0.5, 1) samples, MnO, and MnO_2 were measured to be ~120 mV/decade (Figure S7, Supporting Information).

In order to verify whether the conductivities of the $Li_{2-x}MnP_2O_7$ change as a function of Li contents (x), we measured the conductivity of the four catalysts independently using van der paaw measurement. The measured conductivities of $Li_2MnP_2O_7$, $Li_{1.7}MnP_2O_7$, $Li_{1.5}MnP_2O_7$, and $LiMnP_2O_7$ are 7.780×10^{-11}, 6.109×10, 8.590×10^{-11}, and 6.266×10^{-11} S cm^{-1}, respectively (Figure S8, Supporting Information). These data indicate that the conductivity does not significantly change with the delithiation and cannot account for the dramatic change in the catalytic activity.

In order to check the catalytic stabilities of the $Li_{2-x}MnP_2O_7$ compounds under OER conditions, we performed subsequent potential cycling from 0.7 to 1.5 V versus NHE in 0.5 M sodium phosphate buffer at pH 7.0. The OER and pseudocapacitive currents of $Li_2MnP_2O_7$ and $LiMnP_2O_7$ remained nearly constant, even after 100 cycles, during voltammetry cycling [Figures 5a,b and S2 (Supporting Information)]. $Li_{1.7}MnP_2O_7$ and $Li_{1.5}MnP_2O_7$ also did not exhibit any noticeable change in their currents during voltammetry cycling, indicating their high catalytic stability (Figures S2 and S9, Supporting Information). Moreover, in order to verify whether the surface area of $Li_2MnP_2O_7$ remains constant during the OER, we compared the pseudocapacitive charge storage of $Li_2MnP_2O_7$ during the CV scans. According to previous reports,[47−49] the shaded area during the CV in Figure S10 (Supporting Information) can be estimated to be proportional to the cathodic charge. In our case, the shaded areas of both the first cycle and 100th cycle of $Li_2MnP_2O_7$

dx.doi.org/10.1021/ja410223j | J. Am. Chem. Soc. 2014, 136, 4201−4211

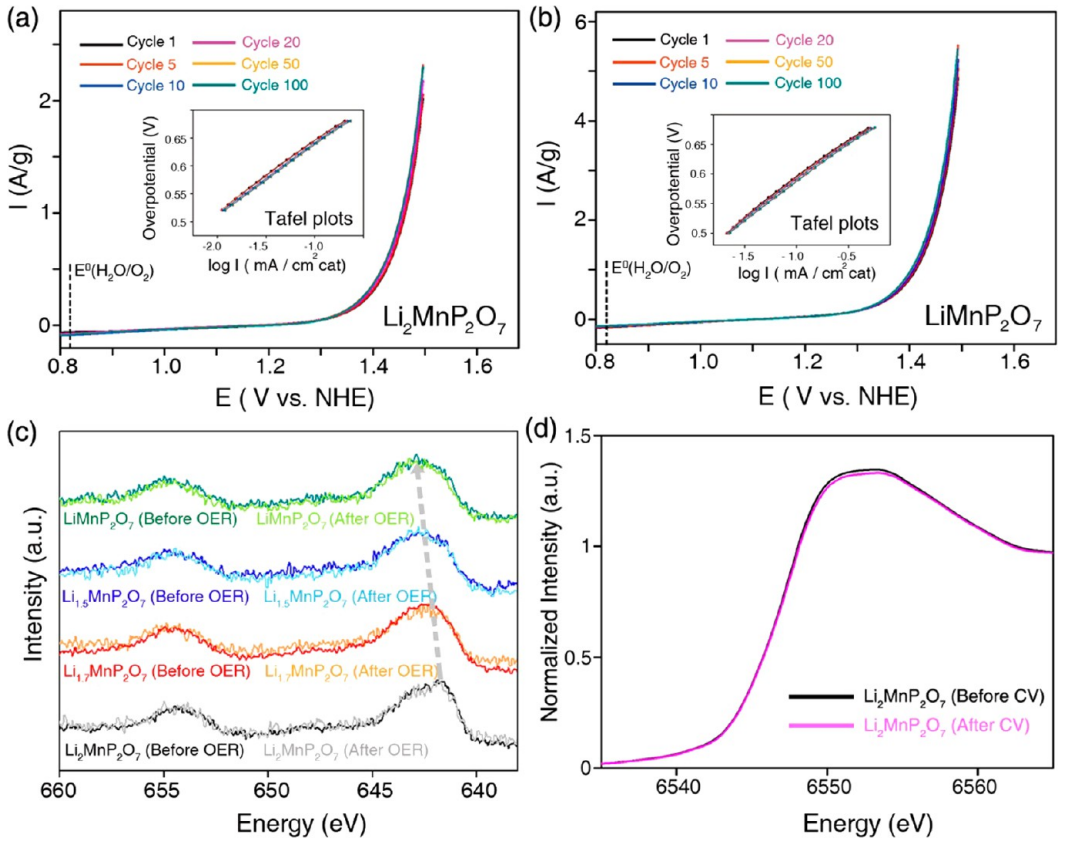

Figure 5. Polarization-corrected cyclic voltammetry curves of $Li_2MnP_2O_7$ (a) and $LiMnP_2O_7$ (b) and their Tafel plots normalized to the surface area of the catalyst (inset) during 100 voltammetry cycles. The thermodynamic potential for water oxidation is marked at 0.816 V vs NHE (pH 7). (c) XPS spectra of the Mn 2p region of as-prepared and bulk-electrolyzed $Li_{2-x}MnP_2O_7$ (x = 0, 0.3, 0.5, 1) at the applied potential of 1.5 V vs NHE for 3 h. The Mn $2p_{3/2}$ peaks of bulk-electrolyzed $Li_2MnP_2O_7$ (gray), $Li_{1.7}MnP_2O_7$ (orange), $Li_{1.5}MnP_2O_7$ (cyan), and $LiMnP_2O_7$ (green) at the surface show similar values as those of the as-prepared samples ($Li_2MnP_2O_7$, black; $Li_{1.7}MnP_2O_7$, red; $Li_{1.5}MnP_2O_7$, blue; and $LiMnP_2O_7$, olive). (d) Ex-situ XANES spectra corresponding to the Mn K-edge of $Li_2MnP_2O_7$ before and after bulk electrolysis at the applied potential of 1.5 V vs NHE for 3 h. All the electrochemical reactions were performed in 0.5 M sodium phosphate buffer at pH 7.0.

normalized to their initial weight onto the FTO substrate are almost identical, indicating that the surface area of $Li_2MnP_2O_7$ remains nearly constant during the OER. Tafel plots of $Li_2MnP_2O_7$ and $LiMnP_2O_7$ in several selected cycles were demonstrated to be almost constant, with a slope value of ~120 mV/decade (Figure 5a,b, inset).

In order to determine whether Li ions leach out during the OER and confirm the stability of all the catalysts, we performed XPS, inductively coupled plasma mass spectrometry (ICP-MS), and ex-situ XANES analysis. We applied 1.5 V versus NHE for 3 h in 0.5 M sodium phosphate buffer at pH 7.0 for each catalyst. First, using XPS, we compared the binding energy of the Mn $2p_{1/2}$ peaks of the as-prepared samples (before the OER) and the bulk-electrolyzed samples (after the OER). Even after 3 h of bulk electrolysis, the peak position of Mn $2p_{1/2}$ remained unchanged compared with the as-prepared samples (Figure 5c). Since the XPS measurement is especially surface-sensitive, the invariance of the XPS Mn peak strongly supports that the oxidation states of Mn both in the bulk and at the surface were maintained without any leaching effect of the Li ion during the OER. Moreover, ICP-MS analysis for the catalysts clearly demonstrates that the ratio of Li ions to Mn ions remained the same after electrolysis (Table S1, Supporting Information). For example, the ratios of Mn to Li ions of $Li_2MnP_2O_7$ and $LiMnP_2O_7$ after electrolysis were 1.99 and 0.99, respectively, indicating that no delithiation occurs during the OER. Additionally, Li ion could not be detected in the electrolyte solution after the bulk electrolysis using ICP-MS analysis. Furthermore, to clearly observe the possible change in the oxidation state of Mn resulting from the delithiation during the OER, we performed ex-situ XANES analysis. The ex-situ XANES spectra corresponding to the Mn K-edge spectra of as-prepared and bulk-electrolyzed $Li_2MnP_2O_7$ were the same, indicating that the oxidation state of Mn ions inside the crystal was maintained during the OER (Figure 5d). This result further supports the finding that delithiation did not occur during the OER. If some portion of Li ions was removed during the OER, the Mn K-edge spectra of electrolyzed $Li_2MnP_2O_7$ would have shifted toward the higher energy region compared with that of as-prepared $Li_2MnP_2O_7$.

Additionally, in order to verify that delithiation of our $Li_2MnP_2O_7$ powders did not occur up to the highest applied potential in our study (1.5 V vs NHE) at room temperature, we conducted cyclic voltammetry and charging−discharging measurements of the powders in a practical battery setup. Briefly, the cathode was formulated by mixing 70 wt % $Li_2MnP_2O_7$, 20 wt % Super P carbon black, and 10 wt % polyvinylidene fluoride (PVDF) binder with a minimal amount of *N*-methylpyrrolidone. Galvanostatic charge−discharge cycling was conducted in the voltage range from 2 to 4.55 V at a rate of C/20. However, it showed negligibly low capacity during charge and discharge, which is well-matched with the previous

dx.doi.org/10.1021/ja410223j | *J. Am. Chem. Soc.* 2014, 136, 4201−4211

report[50] (Figure 6a). Additionally, after voltage cycling of $Li_2MnP_2O_7$ in a practical battery setup, we performed ex-situ

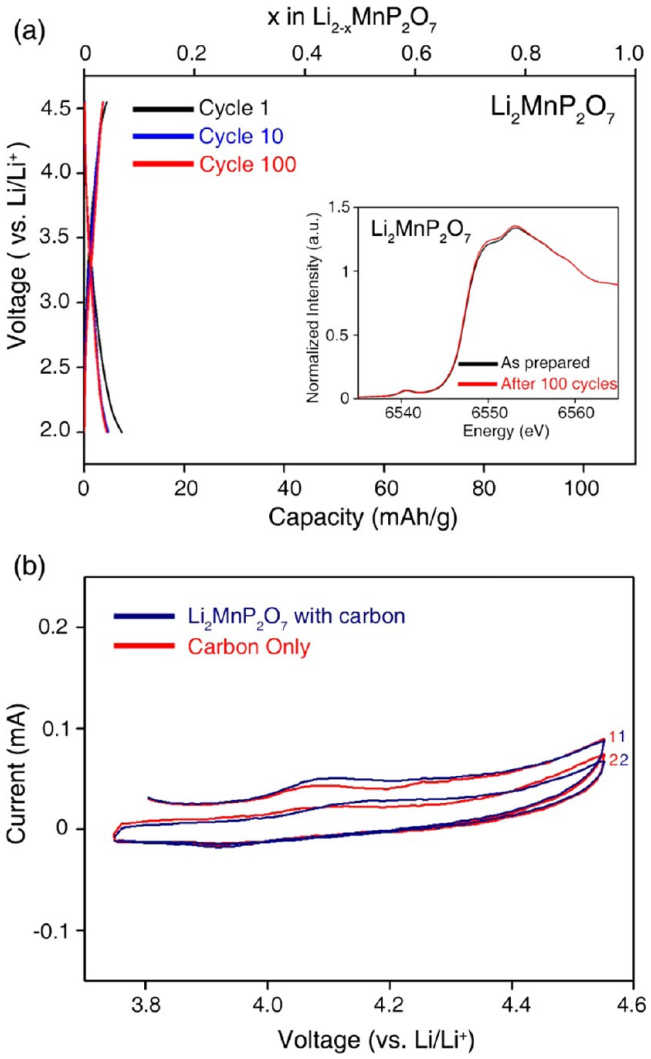

Figure 6. Electrochemical characterization of $Li_2MnP_2O_7$. (a) Galvanostatic voltage−composition curve of $Li_2MnP_2O_7$ at selected cycles (1st, black; 10th, blue; and 100th, red) at a rate of C/20 obtained at 25 °C exhibiting very low capacity and no voltage plateau during charging and discharging. The inset shows that the oxidation state of Mn was not changed after 100 cycles of charging and discharging using ex-situ XANES. (b) Cyclic voltammetry (CV) of $Li_2MnP_2O_7$ paste (blue) and carbon (red) conducted at 10 mV/s and 25 °C.

XANES analysis of the cycled $Li_2MnP_2O_7$ obtained from the electrochemical coin cell. No differences were observed in the ex-situ XANES Mn K-edge spectra of cycled $Li_2MnP_2O_7$ and as-prepared $Li_2MnP_2O_7$, which was also obtained from the coin cell before cycling, further supporting the finding that delithiation does not occur during the OER, even after mixing the catalyst with carbon (Figure 6a inset). We applied potential cycling from 3.75 to 4.55 V vs the Li/Li^+ scale (0.7−1.5 V vs NHE), which is identical to the voltage range during the OER in our study. Under our OER experimental conditions, no distinct reversible cathodic and anodic currents were observed, which clearly indicates that the delithiation of $Li_2MnP_2O_7$ does not occur during the OER (Figure 6b). The very small current (~80 μA) at the applied potential of 4.55 V vs the Li/Li^+ scale is due to the capacitive charge storage of carbon (Figure 6b).

The phase stability of the catalysts during the OER was observed by HRTEM and XRD analysis. The HRTEM images revealed the high crystallinity of the cycled samples both at the surface and in the bulk. The fast Fourier transforms (FFTs) of the HRTEM images can be indexed with the crystal structure of $Li_{2-x}MnP_2O_7$ (Figure 7a,b) [see Figure S11 (Supporting Information) for $Li_{1.7}MnP_2O_7$ and $Li_{1.5}MnP_2O_7$]. XRD analysis also indicates that the phase remained even after 100 cycles, without the appearance of any other phases or any broadening of the peaks (Figure 7c,d).

The valency state and local environments of Mn at the atomistic level was investigated by performing DFT calculations. A series of possible crystal structures of $Li_{2-x}MnP_2O_7$ (x = 0.25, 0.5, 1) and their relative energies were identified which supported its monophasic reaction at room temperature (Figure S12, Supporting Information). We selected the most stable structures in each composition (x = 0.25, 0.5, 1) as the theoretical models of $Li_{1.75}MnP_2O_7$, $Li_{1.5}MnP_2O_7$, and $LiMnP_2O_7$ structures (Figure 8). The charges of Mn in $Li_{2-x}MnP_2O_7$, which were determined using the Voronoi spin integration, were consistent with the XPS results. The average oxidation state of Mn atom gradually changed upon delithiation from 2 to 3. We found that the charges are delocalized among both five- and six-coordinated Mn sites in $Li_{1.75}MnP_2O_7$ (Figure 8b). However, charge localization was observed in $Li_{1.5}MnP_2O_7$, where two of the TBP sites are Mn(III), while only one of the four Oh sites is Mn(III) (Figure 8c). Finally, all of the Mn(II) atoms undergo oxidation to Mn(III) when full delithiation occurs for $Li_2MnP_2O_7$ ($LiMnP_2O_7$) (Figure 8d). Interestingly, in $LiMnP_2O_7$, all the Oh Mn sites transform into TBP by breaking the edge-sharing Mn−O bonds in the Mn_2O_9 subunit (Figure 8d). As a result, delithiation allows all of the Mn ions to be positioned in five-coordinate sites.

From the calculated lattice parameters and the unit-cell volume of $Li_{2-x}MnP_2O_7$ (x = 0, 0.25, 0.5, 1), we could confirm that the changes in the lattice parameters and unit-cell volume were very small; this finding was consistent with experimentally obtained results from XRD analysis (Table S2, Supporting Information). This small change in lattice parameter supports our idea that $Li_{2-x}MnP_2O_7$ can be a good platform for understanding the role of Mn valency in water catalysis with minimal change in structural factors. Moreover, there is negligible volume change, ~1%, between $LiMnP_2O_7$ and $Li_2MnP_2O_7$. Note that the unit-cell volume normalized to the number of total Mn atoms in the unit cell of Mn(II)O is 87.8 $Å^3$/Mn, which is 18.8% smaller than that of $Mn(III)_2O_3$ (104.3 $Å^3$/Mn).

HRTEM analysis of our catalysts shows that the local structure of the surface resembles that of the bulk. Therefore, the atomic structure of the bulk material could be a good platform for a discussion on how Mn valency affects the catalytic effect. Indeed, on the basis of HRTEM analysis, previous reports[22,23,44] selected the atomic structure of each bulk material as a starting point to find the correlations between the crystal structure of the catalysts and their catalytic rate.

The Mn−Mn and Mn−O bond distances for $Li_{2-x}MnP_2O_7$ (x = 0, 0.25, 0.5, 1) were calculated from their theoretical structures. Notably, the average di-μ-oxo Mn−Mn distances and the second Mn−Mn distances were approximately the same among samples of $Li_2MnP_2O_7$, $Li_{1.75}MnP_2O_7$, and $Li_{1.5}MnP_2O_7$. Here, the intermanganese distance, where two

dx.doi.org/10.1021/ja410223j | J. Am. Chem. Soc. 2014, 136, 4201−4211

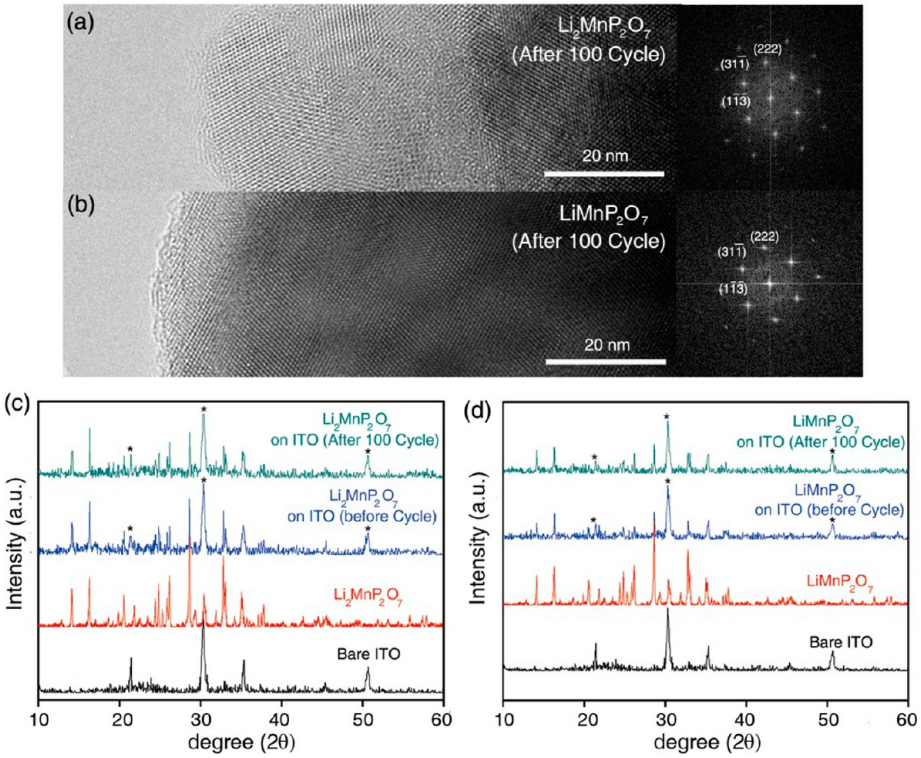

Figure 7. HRTEM images (left) and FFTs (right) of the surface regions of $Li_2MnP_2O_7$ (a) and $LiMnP_2O_7$ (b) after 100 continuous cycles at a scan rate of 10 mV/s from 0.7 to 1.5 V vs NHE in a 0.5 M sodium phosphate buffer at pH 7.0. $Li_2MnP_2O_7$ (c) and $LiMnP_2O_7$ (d) films on an ITO (indium tin oxide) substrate before and after cycling 100 times from 0.7 to 1.5 V vs NHE at 10 mV/s in 0.5 M sodium phosphate buffer at pH 7.0. An asterisk (*) indicates the peak originating from the ITO substrate. All the electrochemical reactions were performed in 0.5 M sodium phosphate buffer at pH 7.0.

Mn atoms are most closely connected by one P_2O_7 group, is notated as the second Mn−Mn distance. For example, the second Mn−Mn distance of $Li_{1.5}MnP_2O_7$ was 5.051 Å, which is only 0.041 Å larger than that of $Li_2MnP_2O_7$ (5.010 Å) (Table 1). The average Mn−O distance of $Li_{2-x}MnP_2O_7$ gradually decreases from 2.183 to 2.033 Å as delithiation proceeds. It is attributed to the oxidation of Mn ions to a higher value with shorter Mn−O bonds.

According to previous studies, the bond distances of Mn−Mn and Mn−O are good indicators for the prediction of catalytic properties. It has been generalized that longer Mn−Mn and Mn−O distances are favorable for OER catalysis.[22,28] The Dismukes group reported that longer and weaker Mn−Mn and Mn−O bond-containing catalysts tend to exhibit better performance.[22] The Dau group also reported that amorphous MnO_x, which has longer Mn−Mn distances, exhibits higher catalytic performance.[28] In our case, we observed that the compound with larger Mn−Mn distance in bulk structures shows higher catalytic ability, which generally agrees with previous works. However, it was noted that changes in the Mn−Mn distance are significantly smaller when considering the large catalytic enhancement. From $Li_2MnP_2O_7$ to $Li_{1.75}MnP_2O_7$ and from $Li_{1.75}MnP_2O_7$ to $Li_{1.5}MnP_2O_7$, the increasing ratios of the average di-μ-oxo Mn−Mn distance were only 1.2% and 0.84%, respectively. These values represent small changes compared to the changes in Mn−Mn distances in conventional Mn oxide compounds. From Mn(II)O to $Mn(III)_2O_3$, the second Mn−Mn distance and the average di-μ-oxo distance increased by 25% and 1.8%, respectively. Here, the second Mn−Mn distances in MnO and Mn_2O_3 refer to the average mono-μ-oxo Mn−Mn distance. Furthermore, the largest change in the Mn−Mn distance was 6.0%, resulting from the change of $Li_{1.5}MnP_2O_7$ to $LiMnP_2O_7$; however, that change does not lead to a greater enhancement of OER during this step. If the Mn−Mn bond distance determines the catalytic activity, the difference between the current densities of $Li_{1.5}MnP_2O_7$ and $LiMnP_2O_7$ should be much larger than that between the current densities of $Li_{1.75}MnP_2O_7$ and $Li_{1.5}MnP_2O_7$, which is gradually enhanced as lithium contents decreased (Figure 4a). We believe that although the effect of the Mn−Mn distance change cannot be completely excluded, it is fair to mention that the Mn−Mn distance change in $Li_{2-x}MnP_2O_7$ remains only a marginal role in the catalytic enhancement.

Previous studies concerning various Mn-containing oxides have suggested that catalysts with weaker and longer Mn−O bonds exhibited higher OER activity than those with stronger and shorter Mn−O bonds.[22,28] However, in our case, we observed that the Mn−O distance in bulk structures decreased from 2.183 Å in low-catalytic $Li_2MnP_2O_7$ to 2.033 Å in high-catalytic $LiMnP_2O_7$. If the Mn−O bond is the dominant factor in the OER activity of $Li_{2-x}MnP_2O_7$, the reduction of the Mn−O bond from $Li_2MnP_2O_7$ to $LiMnP_2O_7$ in the same crystal frameworks might lead to inferior catalytic activity. In this regard, we can conceive that the effect of valency may dominate over structural factors, such as Mn−O or Mn−Mn bond distances in the crystal, in our system.

Moreover, in order to further understand the catalysts' surface structure where the OER occurs, we performed additional DFT calculations from GGA+U. The local Mn atom environment at the most stable surface of each catalyst was found with the well-established surface cleaving method.[51]

dx.doi.org/10.1021/ja410223j | J. Am. Chem. Soc. 2014, 136, 4201−4211

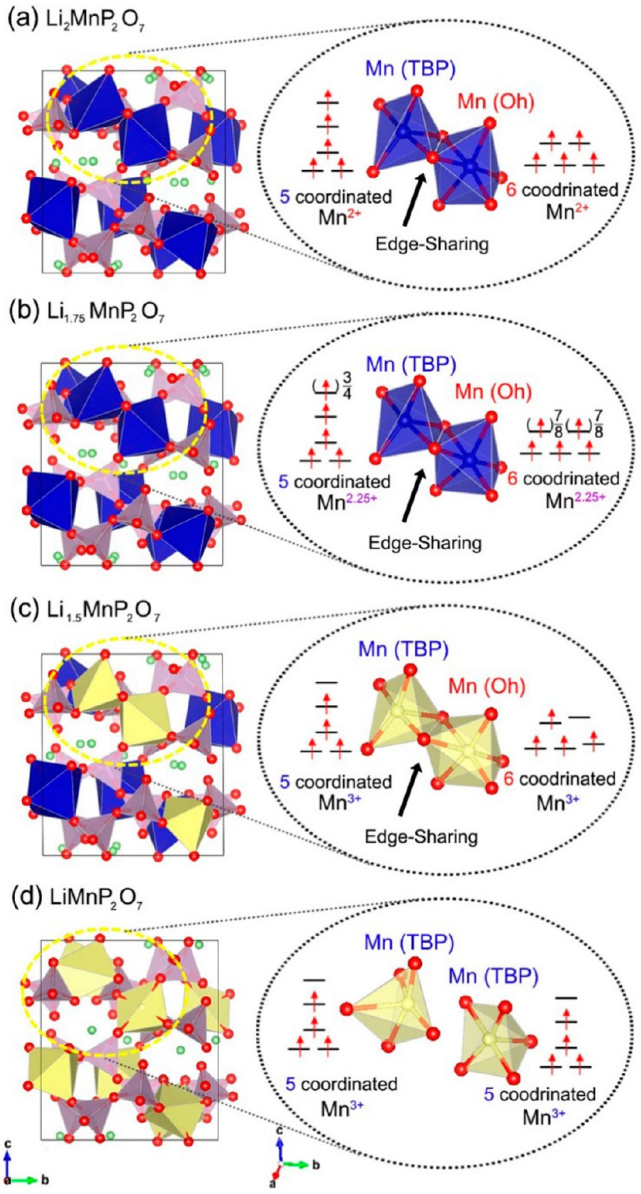

Figure 8. Simulated crystal structures of the $Li_2MnP_2O_7$ (a), $Li_{1.75}MnP_2O_7$ (b), $Li_{1.5}MnP_2O_7$ (c), and $LiMnP_2O_7$ (d) unit cells. The inset shows the local Mn environment around the Mn_2O_9 subunit. Mn^{2+} and Mn^{3+} atoms in the unit cell are shown in blue and yellow, respectively. In $Li_{1.75}MnP_2O_7$, charge delocalization occurs and all of the Mn atoms have an average oxidation state of 2.25; (↑)3/4 and (↑)7/8 indicate that the electron occupancies in each of the orbitals are 3/4 and 7/8, respectively. (b). In $Li_{1.5}MnP_2O_7$, three Mn^{2+} atoms were oxidized into Mn^{3+}, and the remaining five Mn atoms have an average oxidation state of 2.2. (c) All Mn^{2+} is oxidized into Mn^{3+} and all of the Oh Mn sites transforms into TBP (d).

In order to depict the atomic structure of the surface, the atoms near the 10 Å range from the surface were fully relaxed and vacuum slabs of 15 Å were used. Furthermore, water molecules were introduced to the surface to simulate the initial situation of electrolysis near Mn atoms. Note that for the surface of $Li_2MnP_2O_7$ and $LiMnP_2O_7$, empty sites exist where water can be adsorbed. The most stable positions of water molecules at the surface were determined by relaxing the overall structure. The local Mn environment and the water molecules at the surface of $Li_2MnP_2O_7$ and $LiMnP_2O_7$ are shown in Figure 9. All the Mn atoms at the surface of $Li_2MnP_2O_7$ and $LiMnP_2O_7$ have five-coordination when Mn−H_2O bonds form.

On the basis of the calculated surface structures of $Li_2MnP_2O_7$ and $LiMnP_2O_7$, we compared the averaged Mn−O distance and di-μ-oxo Mn−Mn distance around the Mn atoms at the surface (Table 1). The averaged Mn−O distance decreased from 2.173 Å in $Li_2MnP_2O_7$ to 2.008 Å in $LiMnP_2O_7$. Interestingly, the di-μ-oxo Mn−Mn distance decreased from 3.313 Å in $Li_2MnP_2O_7$ to 3.193 Å in $LiMnP_2O_7$. This trend is opposite to that observed in bulk structures of $Li_{2-x}MnP_2O_7$. However, the decreased di-μ-oxo Mn−Mn distance and averaged Mn−O distance at the surface Mn atoms along the delithiation further supports our claim that the Mn−Mn and Mn−O distance change in $Li_{2-x}MnP_2O_7$ might play a marginal role in the enhancement of the catalytic ability.

We believe that the gradually changed Mn valency and occupancy of the d states upon delithiation have affected the catalytic activities of $Li_{2-x}MnP_2O_7$. Previous works indicated that the relationship between e_g occupancy in a transition metal and the 2p level of oxygen-related species (*OH, *O, *OOH) is a crucial factor for the OER activity of a transition-metal-based catalyst.[52,53] Recently, the Dismukes group revealed that Mn-based oxides with e_g^1 orbital generally exhibit high catalytic activity.[22] Moreover, the Rao group emphasized the role of the e_g^1 configuration on water oxidation catalysis using Co^{3+} (t_{2g}^5 e_g^1) and Mn^{3+} (t_{2g}^3 e_g^1) based oxide materials.[54] The change of the Mn valency in the series of $Li_{2-x}MnP_2O_7$ was able to nicely tune the occupation of d states from e_g^2 to e_g^1 and might result in a higher catalysis of water oxidation.

We investigated another possible role of Mn valency from the viewpoint of the asymmetric local Mn environment. Previous studies quantified the degree of Mn polyhedron distortion (Δ),[55] also known as the Baur distortion index, using the following formula

$$\Delta = \frac{1}{N}\sum_{k=1}^{N}\frac{|d_k - d_m|}{d_m}$$

where d_k and d_m are individual Mn−O bond lengths and mean values, respectively, and N is the number of Mn−O bonds in one polyhedron. The distortion indices of Mn polyhedra in

Table 1. Selected Structural Parameters[a] of Calculated $Li_{2-x}MnP_2O_7$ (x = 0, 0.25, 0.5, 1), MnO, and Mn_2O_3

designation	av di-μ-oxo Mn−Mn dist (bulk)	second Mn−Mn dist	av Mn−O dist (bulk)	av di-μ-oxo Mn−Mn dist (surf.)	av Mn−O dist (surf.)
$Li_2MnP_2O_7$	3.302	5.010	2.183	3.313	2.173
$Li_{1.75}MnP_2O_7$	3.343	4.967	2.168		
$Li_{1.5}MnP_2O_7$	3.371	5.051	2.144		
$LiMnP_2O_7$	3.574	4.979	2.033	3.193	2.008
MnO	3.168	4.480	2.265		
Mn_2O_3	3.111	3.578	2.060		

[a]All units are angstroms.

dx.doi.org/10.1021/ja410223j | J. Am. Chem. Soc. 2014, 136, 4201−4211

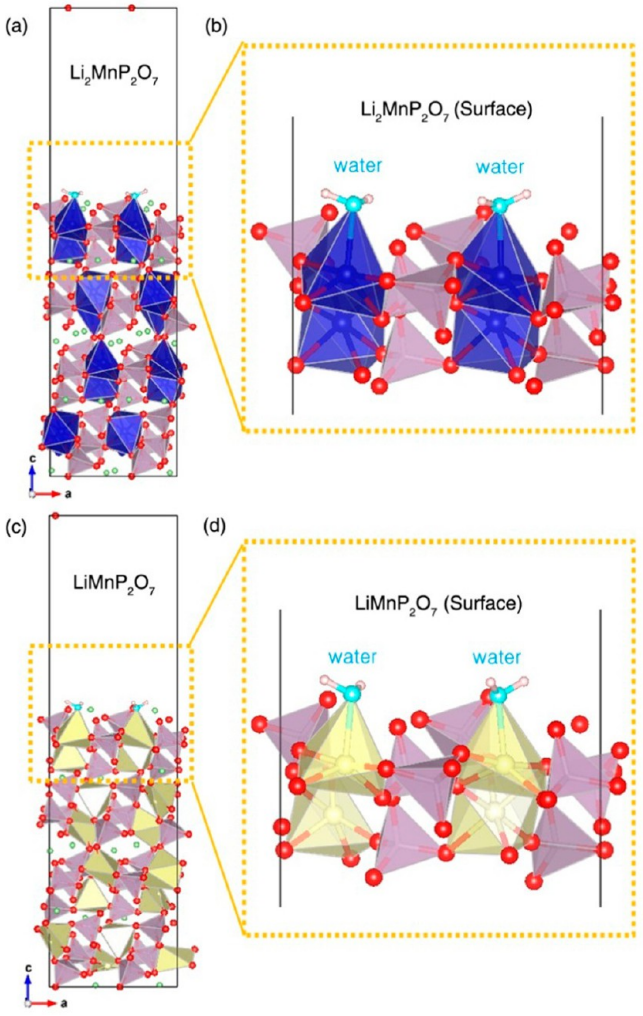

Figure 9. The local environment of the Mn atoms at the surface of $Li_2MnP_2O_7$ (a) and $LiMnP_2O_7$ (c). Magnified images of parts a and c are shown in parts b and d, respectively. The Mn atoms at the surface in $Li_2MnP_2O_7$ and $LiMnP_2O_7$ have open coordination sites where water molecules bind which can serve as the substrate for water oxidation. Mn(II) and Mn(III) atoms and water molecules are indicated in blue, yellow, and cyan, respectively.

$Li_{2-x}MnP_2O_7$ are summarized in Table 2. As the lithium content decreases in $Li_{2-x}MnP_2O_7$, the average distortion index of the Mn polyhedron increases from 0.0191 in $Li_2MnP_2O_7$ to 0.0540 in $LiMnP_2O_7$. This effect occurs because Mn(III) induces Jahn–Teller distortion, which asymmetrically elongates some Mn–O bonds while shortening others. To our surprise, we find that the linear increase in distortion exhibits a trend similar to that of the catalytic enhancement of $Li_{2-x}MnP_2O_7$, as shown in Figure 10. This linear relationship implies that the asymmetric Mn environments affect the catalytic ability of $Li_{2-x}MnP_2O_7$ compounds during water oxidation catalysis.

Table 2. Distortion Index of Calculated $Li_{2-x}MnP_2O_7$ (x = 0, 0.25, 0.5, 1)[a]

	Mn(1)	Mn(2)	av
$Li_2MnP_2O_7$ (bulk)	0.0159	0.0222	0.0191
$Li_{1.7}MnP_2O_7$ (bulk)	0.0240	0.0299	0.0270
$Li_{1.5}MnP_2O_7$ (bulk)	0.0322	0.0440	0.0381
$LiMnP_2O_7$ (bulk)	0.0822	0.0257	0.0540
$Li_2MnP_2O_7$ (surface)	0.0294		0.0294
$LiMnP_2O_7$ (surface)	0.0557		0.0557

[a]Five-coordinated and six-coordinated Mn atoms in the bulk structure of $Li_2MnP_2O_7$ are defined as Mn(1) and Mn(2), respectively. Because only Mn(1) atoms existed at the surfaces, the distortion index of Mn(2) atoms are not shown.

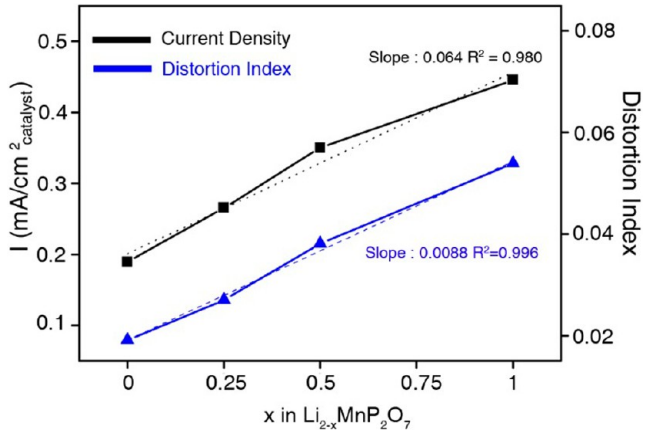

Figure 10. The catalytic current density at the overpotential value of 680 mV (black) and the distortion index value (Δ) (blue) as a function of delithiated amount (x) in $Li_{2-x}MnP_2O_7$. The current density was normalized to the surface area of the catalysts, and the distortion index value was calculated from the definition of the Baur distortion index. The linear trend of both the current density (dashed black line, slope = 0.064, R^2 = 0.980) and distortion index value (dashed blue line, slope = 0.0088, R^2 = 0.996) is clearly shown.

Moreover, we calculated the local distortion index of the Mn atoms at the surface of $Li_2MnP_2O_7$ and $LiMnP_2O_7$. The distortion index of the surface Mn atoms was calculated from the five-coordinated Mn atoms at the surface where Mn–H_2O bonds form. Interestingly, the average local distortion index of Mn atoms at the surface of $LiMnP_2O_7$ (0.0557) shows a higher value than that at the surface of $Li_2MnP_2O_7$ (0.0294). Although the distortion index values at the surface and in the bulk of each catalyst are slightly different, the general trend that the distortion index increases after delithiation is still observed for the surface of the catalysts. This study suggests that the distortion index may serve as a good descriptor for predicting the catalytic ability of Mn-based compounds. However, because $Li_{2-x}MnP_2O_7$ compounds investigated here have unique properties such as trigonal bipyramidal geometry and the loss of edge-sharing bridges upon oxidation, further study on how generally this descriptor can be applied to other systems is needed.

We speculate that the distorted Mn geometry in $Li_2MnP_2O_7$ could contribute to the stabilization of Mn(III) under neutral conditions. It is well-known that the symmetric MnO_6 octahedron in MnO and MnO_2 becomes unstable when Mn(III) is generated during the catalysis; consequently, Mn(III) rapidly dissociates into Mn(II) and Mn(IV) via a charge disproportionation (CD) process under neutral conditions.[29] Thus, an intrinsically distorted crystal structure is favorable for stabilizing the Mn(III) state because the CD process can be suppressed in this structure.[32,41] Indeed, it has been reported that the asymmetric Mn orbital in partially N-doped δ-MnO_2 could stabilize the Mn(III) state under neutral conditions by inhibiting the CD process and consequently

dx.doi.org/10.1021/ja410223j | J. Am. Chem. Soc. 2014, 136, 4201–4211

exhibit excellent OER catalytic behavior.[32] Additionally, we think that the TBP polyhedron in $Li_2MnP_2O_7$ can further stabilize Mn(III) during the catalytic cycle. The TBP polyhedron can be regarded as a highly distorted Oh polyhedron where one Mn−O bond length is exceptionally large to maintain its bond. Because the five-coordinate MnO_5 is not subject to the Jahn−Teller effect,[56] the exchange of Mn valency during catalysis requires a relatively small local change, stabilizing the structure against the CD process.

3. CONCLUSION

In summary, our studies demonstrate the possibility of a new pyrophosphate-based Mn crystal, $Li_2MnP_2O_7$, as an efficient water oxidation catalyst under neutral conditions for the first time. By tuning the manganese valency in $Li_2MnP_2O_7$, we can observe the effect of the Mn(III) state itself on water oxidation catalysis with minimal crystallographic change. $Li_{2-x}MnP_2O_7$ compounds exhibit catalytic stability as high as 1.5 V vs NHE without additional delithiation or phase transformation, ensuring an understanding of the effect of the oxidation state of manganese on water oxidation catalysis based on the catalytic activities. A higher Mn(III) content in the catalyst can boost catalytic activity by increasing the degree of distortion in the local Mn environment both at the surface and in the bulk $Li_{2-x}MnP_2O_7$. We expect that the results highlight the understanding of the effect of the Mn oxidation state on the oxygen evolution reaction and can provide valuable insight for developing a new Mn-based water oxidation catalyst. Moreover, our approach can be applied to construct the design rule for other transition-metal-based (Co, Ni, Fe, Cu) water oxidation catalysts.

■ ASSOCIATED CONTENT

Supporting Information

Full experimental methods, Figures S1−S12, and Tables S1 and S2. This material is available free of charge via the Internet at http://pubs.acs.org.

■ AUTHOR INFORMATION

Corresponding Author

matlgen1@snu.ac.kr; nkitae@snu.ac.kr

Author Contributions

‖These authors contributed equally.

Notes

The authors declare no competing financial interests.

■ ACKNOWLEDGMENTS

This research was supported by Basic Science Research Program through the National Research Foundation of Korea (NRF) funded by the Ministry of Science, ICT & Future (No.Grant Number: 2011-0011225); by the Global Frontier R&D Program on Center for Multiscale Energy System funded by the National Research Foundation under the Ministry of Science, ICT & Future, Korea (0420-20130104); by the Fusion Research Program for Green Technologies through the National Research Foundation of Korea (NRF) funded by the Ministry of Science, ICT & Future (2012M3C1A1048863); by the Supercomputing Center/Korea Institute of Science and Technology Information with supercomputing resources including technical support (KSC-2011-C2-51); by the Human Resources Development program (20124010203320) of the Korea Institute of Energy Technology Evaluation and Planning (KETEP) grant funded by the Korea government Ministry of Trade, Industry and Energy; and by the Research Center Program of IBS(Institute for Basic Science) in Korea.

■ REFERENCES

(1) Lewis, N. S.; Nocera, D. G. *Proc. Natl. Acad. Sci. U. S. A.* **2006**, *103*, 15729.
(2) Gust, D.; Moore, T. A.; Moore, A. L. *Acc. Chem. Res.* **2009**, *42*, 1890.
(3) Swierk, J. R.; Mallouk, T. E. *Chem. Soc. Rev.* **2013**, *42*, 2357.
(4) Bard, A. J.; Fox, M. A. *Acc. Chem. Res.* **1995**, *28*, 141.
(5) Grätzel, M. *Nature* **2001**, *414*, 338.
(6) Barber, J. *Chem. Soc. Rev.* **2009**, *38*, 185.
(7) Meyer, T. J. *Acc. Chem. Res.* **1989**, *22*, 163.
(8) Faunce, T. A.; Lubitz, W.; Rutherford, A. W.; MacFarlane, D.; Moore, G. F.; Yang, P.; Nocera, D. G.; Moore, T. A.; Gregory, D. H.; Fukuzumi, S.; Yoon, K. B.; Armstrong, F. A.; Wasielewski, M. R.; Styring, S. *Energy Environ. Sci.* **2013**, *6*, 695.
(9) Kanan, M. W.; Nocera, D. G. *Science* **2008**, *321*, 1072.
(10) Betley, T. A.; Wu, Q.; Van Voorhis, T.; Nocera, D. G. *Inorg. Chem.* **2008**, *47*, 1849.
(11) Zhao, Y.; Swierk, J. R.; Megiatto, J. D.; Sherman, B.; Youngblood, W. J.; Qin, D.; Lentz, D. M.; Moore, A. L.; Moore, T. A.; Gust, D.; Mallouk, T. E. *Proc. Natl. Acad. Sci. U. S. A.* **2012**, *109*, 15612.
(12) Nakagawa, T.; Beasley, C. A.; Murray, R. W. *J. Phys. Chem. C* **2009**, *113*, 12958.
(13) Tong, L.; Duan, L.; Xu, Y.; Privalov, T.; Sun, L. *Angew. Chem., Int. Ed.* **2011**, *50*, 445.
(14) Sartorel, A.; Carraro, M.; Scorrano, G.; Zorzi, R. D.; Geremia, S.; McDaniel, N. D.; Bernhard, S.; Bonchio, M. *J. Am. Chem. Soc.* **2008**, *130*, 5006.
(15) Joya, K. S.; Subbaiyan, N. K.; D'Souza, F.; de Groot, H. J. M. *Angew. Chem., Int. Ed.* **2012**, *51*, 9601.
(16) Duan, L.; Bozoglian, F.; Mandal, S.; Stewart, B.; Privalov, T.; Llobet, A.; Sun, L. *Nat. Chem.* **2012**, *4*, 418.
(17) Youngblood, W. J.; Lee, S.-H. A.; Kobayashi, Y.; Hernandez-Pagan, E. A.; Hoertz, P. G.; Moore, T. A.; Moore, A. L.; Gust, D.; Mallouk, T. E. *J. Am. Chem. Soc.* **2009**, *131*, 926.
(18) Loll, B.; Kern, J.; Saenger, W.; Zouni, A.; Biesiadka, J. *Nature* **2005**, *438*, 1040.
(19) Yano, J.; Kern, J.; Sauer, K.; Latimer, M. J.; Pushkar, Y.; Biesiadka, J.; Loll, B.; Saenger, W.; Messinger, J.; Zouni, A.; Yachandra, V. K. *Science* **2006**, *314*, 821.
(20) Umena, Y.; Kawakami, K.; Shen, J.-R.; Kamiya, N. *Nature* **2011**, *473*, 55.
(21) Robinson, D. M.; Go, Y. B.; Greenblatt, M.; Dismukes, G. C. *J. Am. Chem. Soc.* **2010**, *132*, 11467.
(22) Robinson, D. M.; Go, Y. B.; Mui, M.; Gardner, G.; Zhang, Z.; Mastrogiovanni, D.; Garfunkel, E.; Li, J.; Greenblatt, M.; Dismukes, G. C. *J. Am. Chem. Soc.* **2013**, *135*, 3494.
(23) Najafpour, M. M.; Ehrenberg, T.; Wiechen, M.; Kurz, P. *Angew. Chem., Int. Ed.* **2010**, *49*, 2233.
(24) Brimblecombe, R.; Kolling, D. R. J.; Bond, A. M.; Dismukes, G. C.; Swiegers, G. F.; Spiccia, L. *Inorg. Chem.* **2009**, *48*, 7269.
(25) Fekete, M.; Hocking, R. K.; Chang, S. L. Y.; Italiano, C.; Patti, A. F.; Arena, F.; Spiccia, L. *Energy Environ. Sci.* **2013**, *6*, 2222.
(26) Jiao, F.; Frei, H. *Chem. Commun.* **2010**, *46*, 2920.
(27) Gorlin, Y.; Jaramillo, T. F. *J. Am. Chem. Soc.* **2010**, *132*, 13612.
(28) Zaharieva, I.; Chernev, P.; Risch, M.; Klingan, K.; Kohlhoff, M.; Fischer, A.; Dau, H. *Energy Environ. Sci.* **2012**, *5*, 708.
(29) Takashima, T.; Hashimoto, K.; Nakamura, R. *J. Am. Chem. Soc.* **2011**, *134*, 1519.
(30) Morita, M.; Iwakura, C.; Tamura, H. *Electrochim. Acta* **1977**, *22*, 325.
(31) Morita, M.; Iwakura, C.; Tamura, H. *Electrochim. Acta* **1978**, *23*, 331.

(32) Takashima, T.; Hashimoto, K.; Nakamura, R. *J. Am. Chem. Soc.* **2012**, *134*, 18153.
(33) Post, J. E. *Proc. Natl. Acad. Sci. U. S. A.* **1999**, *96*, 3447.
(34) Tamaru, M.; Barpanda, P.; Yamada, Y.; Nishimura, S.-i.; Yamada, A. *J. Mater. Chem.* **2012**, *22*, 24526.
(35) Li, G.; Azuma, H.; Tohda, M. *Electrochem. Solid-State Lett.* **2002**, *5*, A135.
(36) Liu, W.; Farrington, G. C.; Chaput, F.; Dunn, B. *J. Electrochem. Soc.* **1996**, *143*, 879.
(37) Kim, H.; Lee, S.; Park, Y.-U.; Kim, H.; Kim, J.; Jeon, S.; Kang, K. *Chem. Mater.* **2011**, *23*, 3930.
(38) Tamaru, M.; Chung, S. C.; Shimizu, D.; Nishimura, S.-i.; Yamada, A. *Chem. Mater.* **2013**, *25*, 2538.
(39) Barpanda, P.; Nishimura, S.-i.; Yamada, A. *Adv. Energy Mater.* **2012**, *2*, 841.
(40) Adam, L.; Guesdon, A.; Raveau, B. *J. Solid State Chem.* **2008**, *181*, 3110.
(41) Sun, Y. K.; Jeon, Y. S.; Leeb, H. J. *Electrochem. Solid-State Lett.* **2000**, *3*, 7.
(42) Klewicki, J. K.; Morgan, J. J. *Environ. Sci. Technol.* **1998**, *32*, 2916.
(43) Wizansky, A. R.; Rauch, P. E.; Disalvo, F. J. *J. Solid State Chem.* **1989**, *81*, 203.
(44) Gardner, G. P.; Go, Y. B.; Robinson, D. M.; Smith, P. F.; Hadermann, J.; Abakumov, A.; Greenblatt, M.; Dismukes, G. C. *Angew. Chem., Int. Ed.* **2012**, *51*, 1616.
(45) Suntivich, J.; Gasteiger, H. A.; Yabuuchi, N.; Shao-Horn, Y. *J. Electrochem. Soc.* **2010**, *157*, B1263.
(46) Lee, S. W.; Carlton, C.; Risch, M.; Surendranath, Y.; Chen, S.; Furutsuki, S.; Yamada, A.; Nocera, D. G.; Shao-Horn, Y. *J. Am. Chem. Soc.* **2012**, *134*, 16959.
(47) Grimaud, A.; May, K. J.; Carlton, C. E.; Lee, Y.-L.; Risch, M.; Hong, W. T.; Zhou, J.; Shao-Horn, Y. *Nat. Commun.* **2013**, 4.
(48) Risch, M.; Grimaud, A.; May, K. J.; Stoerzinger, K. A.; Chen, T. J.; Mansour, A. N.; Shao-Horn, Y. *J. Phys. Chem. C* **2013**, *117*, 8628.
(49) Grimaud, A.; Carlton, C. E.; Risch, M.; Hong, W. T.; May, K. J.; Shao-Horn, Y. *J. Phys. Chem. C* **2013**, *117*, 25926.
(50) Zhou, H.; Upreti, S.; Chernova, N. A.; Hautier, G.; Ceder, G.; Whittingham, M. S. *Chem. Mater.* **2010**, *23*, 293.
(51) Tasker, P. *J. Phys. C: Solid State Phys.* **1979**, *12*, 4977.
(52) Subbaraman, R.; Tripkovic, D.; Chang, K.-C.; Strmcnik, D.; Paulikas, A. P.; Hirunsit, P.; Chan, M.; Greeley, J.; Stamenkovic, V.; Markovic, N. M. *Nat. Mater.* **2012**, *11*, 550.
(53) Chakhalian, J.; Millis, A. J.; Rondinelli, J. *Nat. Mater.* **2012**, *11*, 92.
(54) Maitra, U.; Naidu, B.; Govindaraj, A.; Rao, C. *Proc. Natl. Acad. Sci. U. S. A.* **2013**, *110*, 11704.
(55) Baur, W. *Acta Crystallogr.* **1974**, *B30*, 1195.
(56) Aakesson, R.; Pettersson, L. G. M.; Sandstroem, M.; Wahlgren, U. *J. Am. Chem. Soc.* **1994**, *116*, 8705.